Soft phonon mode dynamics in Aurivillius-type structures

Deepam Maurya,[1,2] Ali Charkhesht,[3] Sanjeev K. Nayak,[4] Fu-Chang Sun,[4] Deepu George,[3] Abhijit Pramanick,[5] Min-Gyu Kang,[1] Hyun-Cheol Song,[1,6] Marshall M. Alexander,[3] Djamila Lou,[3] Giti A. Khodaparast,[3] S. P. Alpay,[4,*] N. Q. Vinh,[3,†] and Shashank Priya[1,2,‡]

[1]*Bio-Inspired Materials and Devices Laboratory (BMDL), Center for Energy Harvesting Materials and Systems (CEHMS), Virginia Tech, Blacksburg, Virginia 24061, USA*

[2]*Institute for Critical Technology and Applied Science (ICTAS), Virginia Tech, Blacksburg, Virginia 24061, USA*

[3]*Department of Physics and Center of Soft Matter and Biological Physics, Virginia Tech, Blacksburg, Virginia 24061, USA*

[4]*Department of Materials Science & Engineering, Department of Physics, Institute of Materials Science, University of Connecticut, Storrs, Connecticut 06269-3136, USA*

[5]*Department of Materials Science and Engineering, City University of Hong Kong, Kowloon, Hong Kong SAR*

[6]*Center for Electronic Materials, Korea Institute of Science and Technology (KIST), Seoul 02792, Republic of Korea*

(Received 6 September 2016; revised manuscript received 14 September 2017; published 18 October 2017)

We report the dynamics of soft phonon modes and their role toward various structural transformations in Aurivillius materials by employing terahertz frequency-domain spectroscopy, atomic pair distribution function analysis, and first-principles calculations. We have chosen $Bi_4Ti_3O_{12}$ as a model system and identified soft phonon modes associated with the paraelectric tetragonal to the ferroelectric monoclinic transition. Three soft phonon modes have been discovered that exhibit a strong temperature dependence. We have determined that the anharmonicity in Bi-O bonds plays a significant role in phonon softening, and that Bi cations play an important role in the emergence of ferroelectricity.

DOI: 10.1103/PhysRevB.96.134114

I. INTRODUCTION

The knowledge of soft phonon mode properties is crucial for understanding the origin of lattice instabilities and structural phase transitions in bismuth layered ferroelectrics (Aurivillius-type structures represented as $[Bi_2O_2][A_{m-1}B_mO_{3m+1}]$, where $m = 3$, $A =$ Bi, and $B =$ Ti, for $Bi_4Ti_3O_{12}$ [BiT]). Typically, ferroelectric-paraelectric phase transitions in these materials occur with the heavily damped phonons in the terahertz (THz) frequencies [1,2]. Additionally, there could be subtle structural distortions below Curie temperature (T_c), which are often difficult to correlate with phonon dynamics. Since structural changes drive many material properties, a fundamental understanding of dynamics of these phonon modes is critical for designing high performance ferroelectric materials and devices [3]. The number of phonon modes is defined by the nature of changes in the symmetry during the transitions. The phase transitions involving more than one soft phonon mode [4] and corresponding order parameters, may induce structural transformations at temperatures below T_c. However, the condensation of more than one phonon mode at a single transition is quite unusual [5]. Using a sensitive and high resolution (HR) THz frequency-domain spectroscope, we have experimentally discovered three elusive phonon modes in the BiT system. These phonon modes, not reported earlier, are expected to have important implications toward the symmetry breaking from the high temperature tetragonal to the low temperature monoclinic phase, as well as structural transformations below the Curie temperature (T_c).

Here, we have employed the BiT as a model system to understand phonon modes related to phase transitions in Aurivillius materials [6]. The ferroelectric members of this family have potential for high temperature sensors and fatigue-free ferroelectric memory devices [7,8]. The structure of BiT consists of a perovskitelike block $(Bi_2Ti_3O_{10})^{2-}$ interleaved with fluoritelike $(Bi_2O_2)^{2+}$ layers perpendicular to the pseudotetragonal c axis [9,10]. BiT undergoes a transition from the high temperature tetragonal paraelectric phase to a lower temperature monoclinic polar phase [11]. This phase transition involves displacement of Bi atoms together with rotation of the TiO_6 octahedra [12].

Much effort has been devoted to understand structural changes with respect to temperature in Aurivillius-family of ferroelectric materials [5,13]. The low temperature ferroelectric monoclinic phase of BiT requires condensation of at least three different symmetry breaking modes, which have hitherto not been observed experimentally [5]. An observation of the temperature dependence of the lowest frequency polar phonon mode (denoted as a soft phonon mode), using Raman scattering is not very convincing, because the intensity of the soft phonon mode decreases rapidly with increasing temperature [4]. Prior studies have investigated the dynamics of the ferroelectric transition in Bi-layered ferroelectric materials using THz time-domain spectroscopy [4,14], where only one optical soft mode was observed in the ferroelectric phase of the BiT material [4]. The mode was underdamped above the phase transition temperature (T_c) due to the change of selection rules in the paraelectric phase. However, in present paper, using a HR and large dynamic range THz frequency-domain spectroscopy [15], we have observed multiple optical modes that could explain the various structural transformations in BiT and BiT-like layered materials. We further employed atomic pair distribution function (PDF) analysis and the first-principles calculations to provide the fundamental understanding of phonon dynamics in layered ferroelectrics.

*Corresponding author: pamir.alpay@uconn.edu
†Corresponding author: vinh@vt.edu
‡Corresponding author: spriya@vt.edu

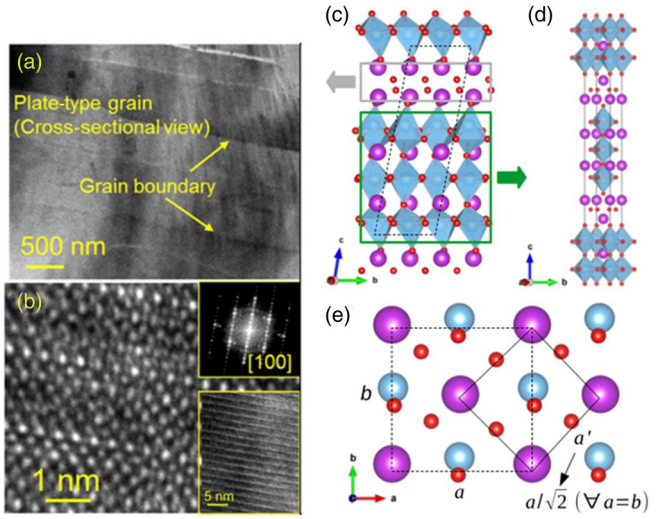

FIG. 1. (a) Bright field cross-section TEM image of plate-type grains in BiT indicates that the thickness is in the range of 200–500 nm. (b) The HR-TEM lattice fringe images of BiT ceramics observed from zone axis [100] indicate the stacking of the pseudoperovskite and $(Bi_2O_2)^{2+}$ layers. The lower inset of (b) shows the corresponding low magnification image. Note that the HR-TEM images, displaying the Bi_2O_3 layers, are collected with the electron beam parallel to the [100] zone axis. The upper inset of (b) depicts the corresponding FFT patterns indicating [100] zone axis. Low and high temperature phases of the BiT structures are shown in (c) and (d), respectively. Bi is denoted by large (purple) spheres and O by small (red) spheres. Ti ions stay at the center of the octahedron surrounded by six O atoms. (e) A suggested transformation path from monoclinic to tetragonal symmetries. This transition is associated with the opposite movement of the fluorite and perovskitelike layers, indicated by arrows (gray and green) shown in (c).

II. EXPERIMENTAL DETAILS

The THz experiments were performed on ⟨001⟩ textured (oriented) BiT ceramics (see Appendix 1–5). For PDF analysis, HR powder x-ray diffraction (XRD) data was recorded using beamline 11-BM at Argonne National Laboratory. Transmission electron microscopy (TEM) images were recorded using the FEI Titan 300 electron microscope. The THz frequency-domain spectrometer consists of a commercial Vector Network Analyzer from Agilent, the N5225A PNA, which covered the frequency range from 10 MHz to 50 GHz, and THz frequency extenders, as well as matched harmonic detectors developed by Virginia Diodes, Inc. with frequency range from 60 GHz to 1.12 THz. The dynamic range of the instrument reaches 10^{13} with a spectral resolution of less than 100 Hz. The details of the THz measurement are described in Appendix 3.

III. RESULTS AND DISCUSSION

Figure 1(a) shows a bright field cross-section TEM image of textured BiT samples. The cross-section morphology indicates that the plate-type BiT grains are stacked along the thickness of the sample, confirming the textured microstructure of the BiT material. From these images, the size of the plate-type grains is in the range of $5-15\,\mu$m (see Appendix 2 on morphology analysis). The thickness of these plate-type grains was found to be in the range of 200–500 nm [Fig. 1(a)]. The stacking of the pseudoperovskite and $(Bi_2O_2)^{2+}$ layers was clearly observed in the HR-TEM lattice fringes from [100] zone axis, as shown in Fig. 1(b). The upper inset in Fig. 1(b) shows the fast Fourier transform (FFT) pattern indicating [100] zone axis, whereas, the lower inset indicates a TEM image with low magnification, revealing a layered structure. Due to the twofold in-plane symmetry, the distinctive stacking of the pseudoperovskite and $(Bi_2O_2)^{2+}$ layers was not observed from [001] zone axis (Appendix 2). The schematic of BiT layered structure at low temperature phase is provided in Fig. 1(c).

The high dynamic range and HR of our THz frequency-domain spectroscopy allow us to observe the lowest-frequency polar phonon modes or soft phonon modes. The refractive index $n(\nu)$ and absorption coefficient $\alpha(\nu)$ of BiT samples have been determined through THz measurements, as shown in Figs. 2(a) and 2(b), respectively, for several temperatures from room temperature to near T_c at 600 °C. The frequency-dependent complex dielectric response, $\varepsilon^*(\nu) = \varepsilon'(\nu) - i\varepsilon''(\nu)$, is related to the complex refractive index, $n^*(\nu) = n(\nu) - i\kappa(\nu)$, through the relations

$$\epsilon'_{\rm sol}(\nu) = n^2(\nu) - \kappa^2(\nu) = n^2(\nu) - (c\alpha(\nu)/4\pi\nu)^2$$
$$\epsilon''_{\rm sol}(\nu) = 2n(\nu)\cdot\kappa(\nu) = 2n(\nu)c\alpha(\nu)/4\pi\nu \qquad (1)$$

where ν is the frequency of the THz radiation. The real part, $n(\nu)$, is the refractive index, and the imaginary part, $\kappa(\nu)$, is the extinction coefficient and indicates the attenuation when the radiation propagates through the material. The extinction coefficient $\kappa(\nu)$ is related to the absorption coefficient through a relation $\alpha(\nu) = \frac{4\pi\cdot\nu\cdot\kappa(\nu)}{c}$, where c is the speed of light.

Accounting for these relationships, we have obtained the complex dielectric response of the BiT sample, including the dielectric loss $\varepsilon''(\nu)$ and permittivity $\varepsilon'(\nu)$ as a function of THz frequency at various temperatures up to the T_c of the material [Figs. 2(c) and 2(d)], respectively. Unlike the previous reports, where only one mode was reported at 0.83 THz [4,7], we have observed three phonon modes at 0.68 THz (22.68 $\rm cm^{-1}$), 0.86 THz (28.69 $\rm cm^{-1}$), and 0.96 THz (32.02 $\rm cm^{-1}$) at room temperature for the 30 μm BiT sample. The observations were reproducible (three different samples) and the temperature cycling did not noticeably affect the observed phonon modes. A strong temperature dependence of these phonon modes and decrease in the corresponding phonon mode frequencies toward zero near the T_c, appear to suggest their soft mode behavior. The theoretical calculations further confirm the soft nature of the observed phonon modes. Upon heating, in addition to mode shifting, the full width at half maximum (FWHM) of the absorption peak also increases with temperature.

To gain better insight into the damping process of the three soft phonon modes, we have fitted the complex dielectric response obtained from our THz frequency-domain spectroscopy at various temperatures. For this, we have employed a function containing a sum of three damped Lorentz oscillators describing the optical phonons of the

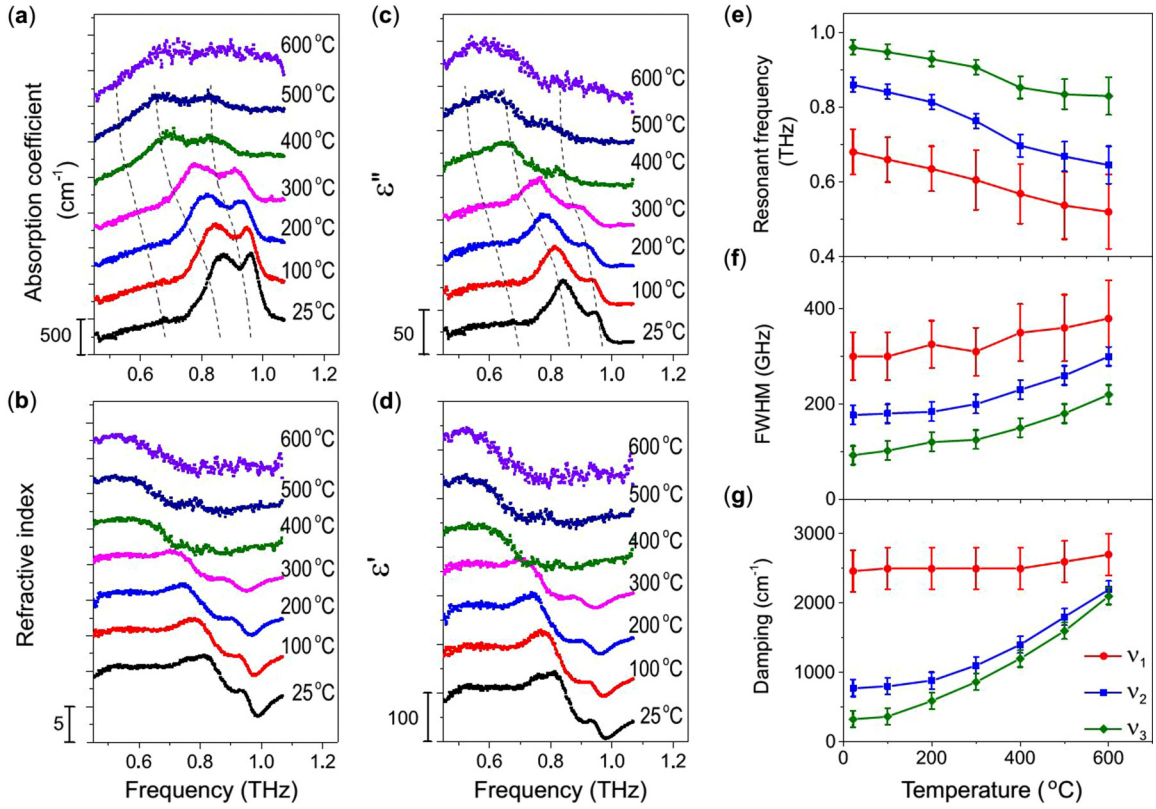

FIG. 2. The THz (a) absorption and (b) refractive index of the c oriented textured polycrystalline BiT ceramic material recorded at various temperatures. Complex THz dielectric response including (c) the dielectric loss and (d) the permittivity at different temperatures calculated from their absorption and refractive index. Employing the three-damped oscillator model, we extracted values for (e) soft optical phonon frequencies ν_1, ν_2, and ν_3, (f) FWHM and (g) phonon damping factors γ_1, γ_2, γ_3. The curves are shifted for clarity in panels (a)–(d), and the dashed lines are guides for the eye.

ferroelectric materials [16]

$$\varepsilon^*(\nu) = \varepsilon_\infty + \sum_{j=1}^{3} \frac{A_j/(2\pi)^2}{\nu_j^2 - \nu^2 + i\nu(\gamma_j)} \tag{2}$$

where $A_j/(2\pi)^2$, ν_j, and γ_j are, respectively, the spectral amplitude of the j damped resonances, its frequency, and its damping coefficient, ε_∞ describes contributions to the dielectric function from modes at frequencies much greater than our experimental range. The parameters of three soft-phonon modes as a function of sample temperature are summarized in Figs. 2(e)–2(g). The resonant frequencies of the three soft phonon modes (ν_1, ν_2, and ν_3) decreases with increasing sample temperature. The damping of these modes increases with the sample temperature. Specifically, while the damping and FWHM values for the ν_1 phonon mode slightly change with the sample temperature, these parameters for the ν_2 and ν_3 modes exhibit a strong increase with increasing temperature, suggesting a finite coupling between these modes. The results are an indication of the soft nature of these phonon modes.

The pronounced softening of the ν_2 and ν_3 modes with increasing temperature can be understood as a result of impending ferroelectric-to-paraelectric phase transition as the sample temperature approaches $T_c \sim 660\,^\circ$C. This is shown by combining the THz spectroscopy with the atomic PDF measurements and the first-principle calculation. The anomalies below T_c could be observed from the THz spectra, as shown in Fig. 2. A discontinuity in the temperature dependence and a sharp increase in FWHM for all these modes occur at $T > 300\,^\circ$C. The damping of these phonon modes increase significantly when the sample temperature reaches near T_c. To understand the possible structural distortions, which might explain anomalies observed below T_c, we performed the atomic PDF measurements. The PDF results obtained from a total scattering XRD pattern via a Fourier transform provide us an approach to study the local structure of materials. Because the total scattering pattern is composed of Bragg, as well as diffuse scattering contributions, the information contains local, medium range, and long range structure information. The high energy XRD results were corrected for the sample absorption, background, Compton scattering, and incident flux. The intensities were normalized and reduced to the structure factor $S(Q)$ (where Q is the diffraction wave vector), which was Fourier transformed to the corresponding PDFs using PDFgetX [17], $G(r)$ (see Appendix 4). The $G(r)$ gives the probability of finding a pair of atoms at a distance r [18]:

$$G(r) = \frac{2}{\pi} \int_0^\infty Q[S(Q) - 1] \sin(Qr) dQ \tag{3}$$

Having the experimental PDF, one can determine local structural changes. The PDF results were fitted with $B2cb$ structure having lattice parameters $a = 5.448$ Å, $b = 5.411$ Å,

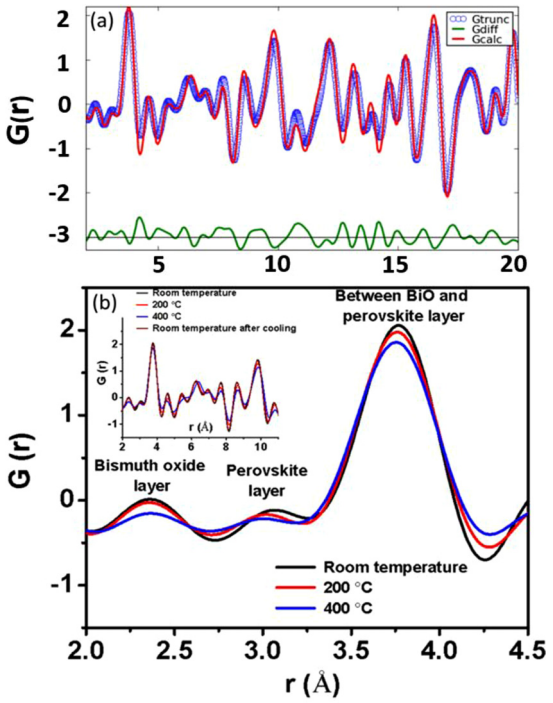

FIG. 3. (a) The fit obtained using PDFGUI for $B2cb$ structure in BiT. (b) Peaks indicate the closest neighbor Bi-O bonds. The Bi-O bonds show significant disordered structure at higher temperatures for both bismuth oxide and the perovskite layers. The inset of Fig. 3(b) shows the PDFs, $G(r)$, measured under different conditions, providing a relation between the dynamics of Bi ions with phonon dynamics. The calculated pattern for the $B2cb$ structure is plotted with dotted line, which merges with the measured data at room temperature.

$c = 32.83$ Å, as shown in Fig. 3(a). The atomic positions were the same as given by Rae *et al.* [19]. The peaks for the nearest neighbors are highlighted in Fig. 3(b). The inset of Fig. 3(b) shows the experimental PDF, $G(r)$, for BiT at different conditions. One can clearly see the broadening of the peaks related to the bismuth oxide layer and perovskite layer at 400 °C [Fig. 3(b)]. The broadening of these peaks indicates increasing disorder in bismuth layers. Most notably, the peak related to the perovskite layer is not just broadened, but also, became asymmetric indicating increased anharmonicity of the Bi-O bonds. We have determined that the anharmonicity of these bonds plays a significant role in shifting of the soft phonon modes and could possibly be the origin of anomalies observed in THz spectra below T_c.

To obtain further insight into the experimentally observed phonon dynamics and bond anharmonicity, phonon studies were performed with first-principles density functional theory (DFT) [20,21]. The generalized gradient approximation [22] was used as the exchange-correlation functional together with the projector-augmented wave method [23], as implemented in the Vienna *Ab initio* Simulation Package (VASP) [24–26]. The primitive cell dimensions for the monoclinic BiT (Table I) were found to be in good agreement with experimental reports [27] and other first-principles computations [11,28]. Our phonon calculations were performed by the linear response method [29] and the frozen phonon method together with Phonopy [30]. The combination of DFT with a frozen phonon method provides the platform to analyze lattice dynamics in quasiharmonic approximation with the interatomic forces calculated from the state-of-the-art electronic structure methods.

TABLE I. Table showing the lattice parameters of various models considered in this study. Here, a, b, and c are lattice parameters (Å); α_0 (deg) and V_0 (Å^3/unit cell) are the monoclinic lattice angle and volume for the ground state crystal structure, respectively.

	Volume	a	b	c	α	β	γ
DFT (present)	506.252	5.493	5.533	16.883	80.609	90	90
1.004 α_0	506.252	5.450	5.522	17.034	80.933	90	90
1.007 α_0	506.252	5.436	5.525	17.060	81.148	90	90
1.015 V_0	513.884	5.521	5.560	16.968	80.609	90	90
1.03 V_0	521.592	5.548	5.588	17.052	80.609	90	90
Tetragonal	492.676	3.852	3.852	33.197	90	90	90
Ref. [19]	486.652	3.85	3.85	32.832	90	90	90

The phonon density of states (DOS) is shown as a black solid line in Fig. 4. We identified three peaks P1, P2, and P3 in the range 0.6–1.5 THz. The phonon band structure shown in Fig. 5 indicated that P2 could be matched to two phonon modes at the Γ point that were almost degenerate, and P3 is the next optical mode. The phonon band diagram was established by appropriately expanding the size of the supercell along a, b, and c lattice vectors to account for all the commensurate k points along x (Γ-Y), y (Γ-Z), and z axes (Γ-B) of the Brillouin zone. To determine the complete band diagram, a supercell of size up to $8 \times 8 \times 4$ unit cells, consisting of 9728 atoms, is required, which is not computationally feasible. The eigenvalues of three low energy phonons, obtained from density functional perturbation theory (DFPT), using the $2 \times 2 \times 1$ supercell, were found

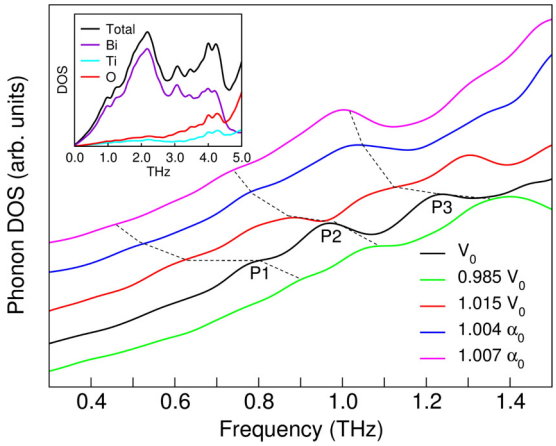

FIG. 4. The phonon DOS for the ground state monoclinic structure (V_0) is shown as black line. The DOS for volume change −1.5% (0.985 V_0) and +1.5 (1.015 V_0) are shown as green and red lines, while that for change in lattice angle α by 0.4% (1.004 α_0) and 0.7% (1.007 α_0) are shown as blue and magenta solid lines, respectively. The peaks shift to lower frequencies in all cases due to deviation from the ground state lattice. The DOS is shifted for clarity. The dashed lines are guide to the eye. The inset shows atomic contribution to the total phonon DOS, suggesting that a major contribution to phonons in the low energy range is from Bi atoms.

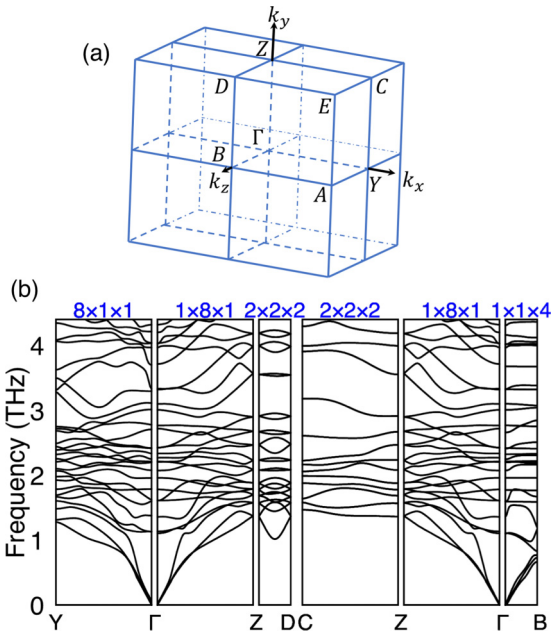

FIG. 5. (a) Brillouin zone and (b) the phonon band structure for the monoclinic BiT lattice. The appropriate size of supercell is chosen as shown in the top panel to incorporate the commensurate k points along the high-symmetry path.

to be 1.11, 1.13, and 1.26 THz. These modes were infrared active and had symmetries A'', A', and A' (verified with the Quantum Espresso code). To observe the effect of volume change, we computed the phonon DOS with a volume change of $+1.5\%$ V_0 and -1.5% V_0, shown as red and green lines in Fig. 4, respectively. We also explored the effect of octahedral tilting on the phonon DOS by increasing the monoclinic angle α_0 by 0.4 and 0.7%, as shown in Fig. 4 in blue and magenta lines, respectively. It is important to note that the DOS of the models are shifted in y axis to compare the plots. The y shift does not have a physical meaning. The crystal structure parameters for various models used in this study are tabulated in Table I. These results suggested that the phonon peaks were shifted to lower frequencies for the models deviating from the ground state monoclinic structure. The peak P2 appeared to split the constituting phonon modes by about 0.2 THz when the volume was increased. Upon reduction of the volume to 0.985 V_0, the phonons were found to exhibit hardening behavior. Thermodynamic analysis from Phonopy suggests the volume increases up to a certain temperature and then starts decreasing with increasing temperature (see Appendix 6). This is consistent with the larger crystallographic volume of the ferroelectric monoclinic phase, as compared to the paraelectric tetragonal phase of BiT, because, the monoclinic phase of BiT has larger volume (252.13 Å^3/unit cell) than that of the tetragonal phase (246.34 Å^3/unit cell) of BiT [31]. In order to study the soft phonon characteristics, the modes obtained for the lowest four phonon energies from DFPT calculations have been subject to variation of amplitude and the total energy of the supercells calculated using VASP, as shown in Fig. 6. The models with pure monoclinic lattice (α_0) and lattice with $\alpha = 1.004\ \alpha_0$ and $\alpha = 1.007\ \alpha_0$ were chosen, as these models were adapting from monoclinic toward the tetragonal structure.

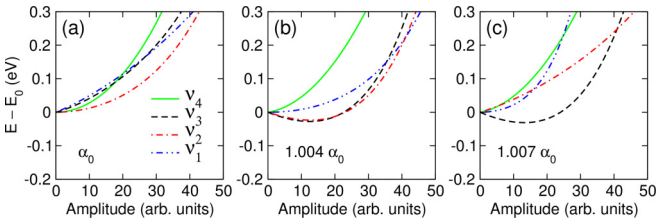

FIG. 6. Total energy as a function of amplitude for the lowest four phonon modes for (a) perfect monoclinic structure, (b) monoclinic lattice with $\alpha = 1.004\ \alpha_0$ and (c) monoclinic lattice with $\alpha = 1.007\ \alpha_0$, respectively. The lowering in energy as a function of amplitude is a signature nature of soft phonon mode.

The lowering in energy as a function of amplitude is found for two modes for $\alpha = 1.004\ \alpha_0$. With an increase of α to $1.007\ \alpha_0$, one of the two modes recover, while the other undergoes further reduction in energy. The minima in these curves are 27.4 and 31.0 meV for $1.004\ \alpha_0$ and $1.007\ \alpha_0$ models, respectively. The lowering in energy as a function of amplitude is a sigature nature of the soft phonon mode. These results indicated that atomic rearrangement accommodating the changes in the unit cell could lead to anharmonicity in the interatomic bonds, as observed in the PDF analysis of Fig. 3.

The phonons at P2 and P3 of Fig. 4, show vibration of ions in the perovskite and fluorite blocks (see Supplemental Material for animated gif files of the phonon modes [32]). The correlated motion of atoms within each block, which are out-of-phase with respect to each other, is shown in the gray and green regions in Fig. 1(c). The out-of-phase oscillations of the lattice blocks could potentially lead to the deviation from the monoclinic toward tetragonal phase [Fig. 1(d)]. The structural change could be described using the lattice parameter transformation $a < b \ \rightarrow a' = b'$, such that the lattice parameter of the tetragonal phase is $a'(=b') \ = a/\sqrt{2}$ [Fig. 1(e)]. This mechanism is consistent with the theoretical findings of Ref. [3], where it is formulated that two unstable E_u modes in BiT, (in which, one is attributed to the motion of fluorite layers in a direction relative to the perovskite $(TiO_6)^{8-}$ blocks and the second mode is related to the motion of the Bi ions in the perovskite A site, with respect to the perovskite blocks), are responsible for the phase change. The atomic displacements in the fluorite layers are found to be larger than in the perovskite layers. Thus, we emphasize that the chemical nature of the large cation in the fluorite layers in the Aurivillius family and similar layered oxides is crucial for structural transformations. We note, however, that the theoretical tools used here could have certain limitations when applied to more complicated crystal structures. First, the quasiharmonic approximation is not appropriate for larger scale volume and/or angular variations. In addition, this approach may not be employed to accurately determine phase transformation temperatures in strongly correlated systems. Future improvements on the current theoretical foundations will, therefore, be necessary to describe more complex systems.

IV. CONCLUSIONS

In summary, we have probed dynamics of soft phonon modes and its role in the structural transformations on ⟨001⟩ oriented BiT using the THz frequency-domain spectroscopy.

The results from the THz frequency-domain spectroscopy have revealed three low frequency soft phonon modes, which have been supported from first-principles study and the atomic PDF analysis. The anharmonicity of the Bi-O bonds plays a leading role in these low frequency phonon modes where the, majority of the contribution to the phonon DOS originates from the Bi atoms. A fundamental understanding about the various factors affecting the observed phonon dynamics and structural changes, described here provide useful information in designing tailored phase transitions and functionality (e.g., ferroelectric and thermal properties) of layered-structure ferroelectric materials.

ACKNOWLEDGMENTS

This paper was supported by the Air Force Office of Scientific Research (AFOSR) through Grant No. FA9550-14-1-0376. The THz-dielectric research was supported by the Institute of Critical Technology and Applied Sciences (ICTAS) at Virginia Tech. M.G.K. and H.C.S. acknowledge financial support through the US Department of Energy Program (Grant No. DE-FG02-06ER46290). The computational resources from the Taylor L. Booth Engineering Center for Advanced Technology (BECAT) at University of Connecticut are gratefully acknowledged. F.-C.S. thanks J. Skelton, University of Bath, and H. Tran and K. Pitike from the University of Connecticut for helpful discussions. S.K.N. acknowledges technical support from Serge M. Nakhmanson, University of Connecticut, and Waheed A. Adeagbo, Martin Luther University Halle-Wittenberg. Use of the Advanced Photon Source at Argonne National Laboratory was supported by the US Department of Energy, Office of Science, Office of Basic Energy Sciences, under Contract No. DE-AC02-06CH11357. A.P. gratefully acknowledges funding support from CityU Start-Up Grant for New Faculty (Project No. 7200514). S.P. acknowledges the support from the National Science Foundation (NSF), Centers of Research Excellence in Science and Technology (CREST) program through Grant No. HRD 1547771.

A.C. and S.K.N. contributed equally to this work.

APPENDIX

1. Sample preparation

To synthesize textured BiT ceramics, we first synthesized BiT platelets using the molten salt synthesis method [33]. For this, stoichiometric amount of Bi_2O_3 and TiO_2 ceramics were ball milled for 24 h under ethyl alcohol in polyethylene bottle with yttria-stabilized zirconia (YSZ) balls as milling media. This slurry was further dried in an oven at 60 °C for 6 h. The resulting powder was mixed with an equal amount of salt mixture (56 wt% KCl and 44 wt% NaCl) and heated at 1150 °C for 30 min. Next, this product was washed several times in deionized water to remove salt and obtain BiT platelets. These platelets were pressed to obtain a cylindrical pellet and sintered at 1150 °C for 2 h. Furthermore, during high temperature processing, all the specimens were muffled with the powder of the same composition to maintain the chemical composition. During pressing, the anisotropic BiT particles with large aspect ratio were aligned with the major surface perpendicular to the pressing direction, which resulted in textured BiT ceramics after sintering.

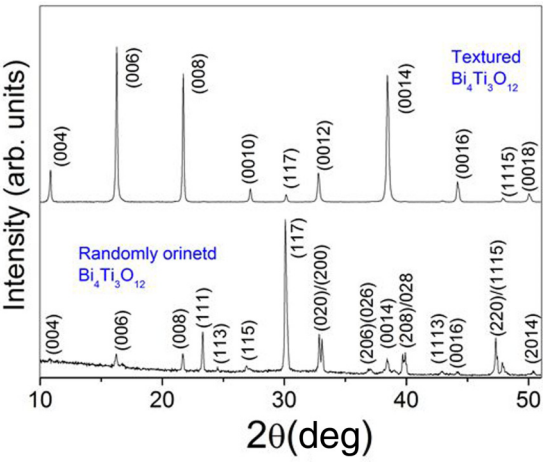

FIG. 7. The XRD spectra recorded at room temperature for textured and randomly oriented BiT ceramics. Please note the change in the intensity of textured BiT ceramics indicating high degree of the crystallographic orientation along *c* axis.

2. Texture and microstructure

Room temperature XRD spectra were recorded by using a Philips Xpert Pro x-ray diffractometer (Almelo, The Netherlands). These XRD patterns clearly suggest formation of pure BiT phase. The change in the intensity of Bragg reflections in the XRD spectrum of textured BiT clearly suggests a high degree of texturing. The degree of orientation was determined from the XRD pattern of the textured BiT in the range of $2\theta = 10-50°$ by Lotgering's method. The Lotgering factor f is defined as the fraction of area textured with required crystallographic plane using the formula [34]:

$$\text{Lotgering factor } f_{00l} = \frac{P - P_o}{1 - P_o}, \quad P = \frac{\Sigma I(00l)}{\Sigma I(hkl)}, \quad P_o = \frac{\Sigma I_o(00l)}{\Sigma I_o(hkl)} \tag{A1}$$

where I and I_o are intensities of the diffraction lines (hkl) of textured and randomly oriented specimens, respectively. The degree of texturing (calculated using Lotgering factor) was found to be 96% suggesting sintered ceramics are oriented along the *c* axis.

The surface morphology of the sintered samples was observed using a LEO Zeiss 1550 (Zeiss, Munich, Germany) scanning electron microscope (SEM). To prepare the electron transparent TEM specimens, we used standard grinding and ion-milling method. For conducting TEM, we used a FEI Titan 300 microscope.

Figure 7 shows XRD-patterns recorded at room temperature for textured BiT ceramics. The change in the intensity of various Bragg reflections compared to randomly oriented counterpart, suggests a high degree of texture along the *c* axis. The Lotgering factor f_{00l} calculated from these XRD patterns suggested 96% texturing in a ⟨001⟩ orientation. To investigate the morphology of the textured BiT samples, SEM micrographs were recorded on the flat surface [Fig. 8(a)]. The flat surface clearly shows a plate-type (major surface in the plane of the sample's top surface) grain morphology. From these images, it can be seen that the size of the plate-type grains

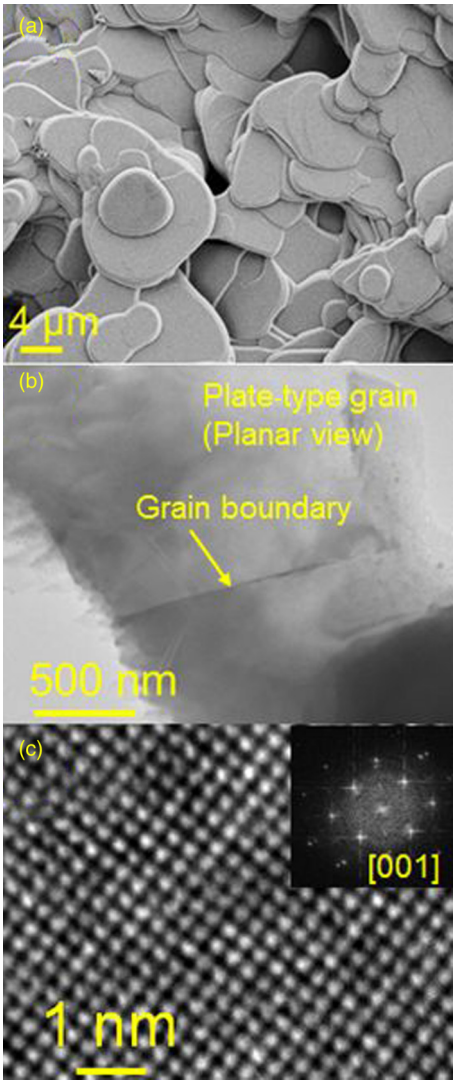

FIG. 8. (a) The SEM micrographs of ⟨001⟩ textured BiT from top surface. (b) Bright field TEM image of the plate-type grains from the top surface. (c) The HR-TEM lattice fringe images of BiT ceramics from [001] zone axis. The inset of (c) shows FFT patterns marked with the zone axes.

was in the range of 5−15 μm. Figures 8(b) and 8(c) show the bright field cross section TEM micrographs of a plane view samples. The grain boundaries in textured BiT are the result of fusing BiT plates together (during a high temperature sintering process) mostly with a slight misorientation. Figure 8(c) show a HR-TEM image of the lattice fringes from [001] orientation. Due to the twofold in-plane symmetry, the distinctive stacking of the pseudoperovskite and $(Bi_2O_2)^{2+}$ layers was not observed. Moreover, the layered structure of these materials was found to be useful in decreasing the thermal conductivity due to effective phonon scattering [8].

3. The THz measurements

The details of the THz spectrometer measurements can be found elsewhere [15]. The spectrometer supports the simultaneous measurements of absorbance and refractive index of specimens over the spectral range from 26.5 GHz

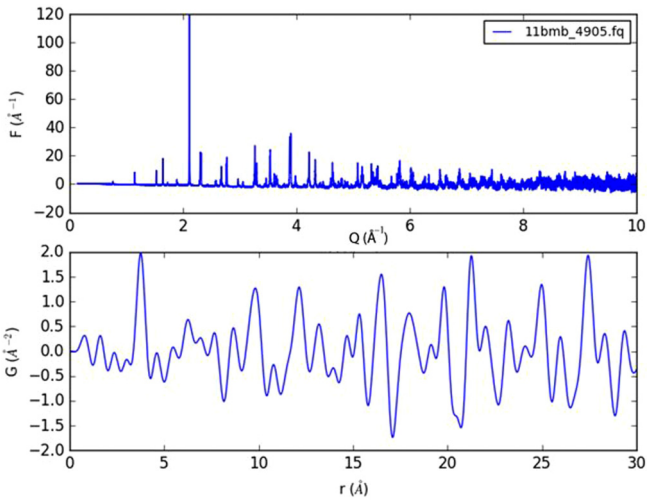

FIG. 9. $F(Q)$ and $G(r)$ profiles for BiT from PDFgetX [17].

to 1.12 THz (0.88 to 37.36 cm^{-1} or 0.268 to 11.3 mm). The signal-to-noise and spectral resolution of this instrument are significantly high as compared to any previous state-of-the-art instruments. For example, while the dynamic range of a commercial THz time-domain spectrometer is about 10^6 and its spectral resolution is several gigahertz, the dynamic range of our instrument reaches an unprecedented value of 10^{13}, and the system achieves a spectral resolution of less than 100 Hz [15,16,35,36]. The system provides a coherent radiation source with a power up to 20 mW in the gigahertz-to-THz region.

For transmission measurements, we employed a quasioptical setup. The transmitter module emits THz radiation into free space with a circular horn. The radiation transmitted through the sample was subsequently collected using a similar horn and was fed into a receiver module. For temperature dependent measurements, we used a home built temperature controllable setup made of a horizontal solid tube furnace from Thermcraft with 1200 °C maximum temperature. Temperature of the sample was controlled with an accuracy of ±10 °C, by varying the voltage applied to the tube furnace. The BiT film was placed on a stainless steel sample holder using thermal paste and was attached to an aperture of the tube furnace. An identical aperture and empty sample holder formed reference signals. The translation stage allowed alternative reference and sample measurements under identical conditions. The high dynamic range combined with the ability to detect the phase allowed accurate measurements of absorption coefficient and refractive index of highly absorptive samples like BiT. The experiment was consisted of two consecutive measurements for each temperature: (i) the reference signals of transmitted intensity and phase shift with an empty sample holder; (ii) the intensity and phase shift with the BiT sample.

4. Atomic PDF

The atomic PDF analysis can be used to understand local structural changes. The PDFgetX was used to compute $G(r)$ from the XRD data recorded on BiT, as shown in Fig. 9. The Q_{maxinst} was limited to 10 Å^{-1} due to the increased noise. The wavelength used for calculations was 0.414211 Å.

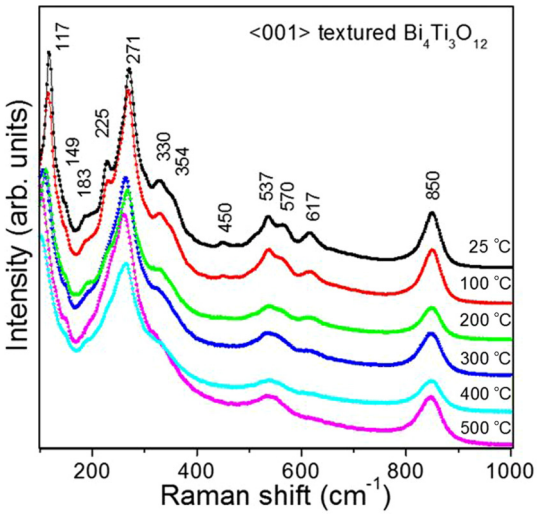

FIG. 10. Raman spectra versus temperature for BiT. The observed variations in frequency and intensity of various modes are the indications of the structural changes with increasing temperature.

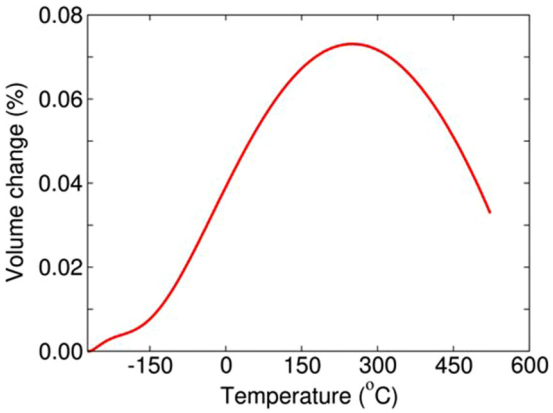

FIG. 11. Temperature dependence of the crystallographic volume change for BiT, obtained from the quasiharmonic approximation.

5. Temperature dependent Raman spectra

Raman measurements were conducted at the Virginia Tech Vibrational Spectroscopy Laboratory using a Jobin-Yvon HR800 Raman microprobe equipped with a 514 nm laser focused onto the sample through a microscope lens. Machado *et al* [31]. reported two unstable E_u modes in BiT, one involving the motion of $(Bi_2O_2)^{2+}$ layers in a direction relative to the perovskite blocks and the second one involving the motion of the Bi ions in the perovskite at A site with respect to the TiO_6 perovskite blocks. The unstable E_u mode in layered materials involving movements of $(Bi_2O_2)^{2+}$ layers with respect to the perovskite block is a general feature of the Aurivillius compounds [31]. These modes occur at a very low frequency zone of center optical phonons, in which layers move as rigid units. The remaining unstable mode in BiT has, however, a completely different displacement pattern. To understand phonon dynamics and the local structural changes with temperature, the temperature dependent Raman spectra (Fig. 10) were recorded.

The heavy Bi ions are expected to exhibit their contribution in the lower frequency regime. The softening of modes at 117 and 271 cm^{-1} can be treated as a signature nature that the system undergoes structural transitions. Modes above 200 cm^{-1} stem from TiO_6 octahedra. The Raman modes at 850, 617, 570, and 330 cm^{-1} and 450 and 354 cm^{-1} are assigned to A_{1g} and B_{1g} modes, respectively. The modes at 537, 271, and 225 cm^{-1} are assigned to $B_{2g} + B_{3g}$ modes originating from the lifting of E_g degeneracies. The disappearance and changes in the modes at 617, 570, 450, 330, 225, and 183 cm^{-1} are believed to be due to the reconstructions in overcoming the distortion and octahedral tilting. These changes hint the nanoscale structural changes in the system, which could be the precursors for the structural transformation at the (T_c).

6. Unit cell volume versus temperature

Figure 11 shows the temperature dependence of the volume change of monoclininc BiT obtained from quasiharmonic approximation.

[1] J. Hlinka, T. Ostapchuk, D. Nuzhnyy, J. Petzelt, P. Kuzel, C. Kadlec, P. Vanek, I. Ponomareva, and L. Bellaiche, Phys. Rev. Lett. **101**, 167402 (2008).

[2] D. Wang, A. A. Bokov, Z. G. Ye, J. Hlinka, and L. Bellaiche, Nat. Commun. **7**, 11014 (2016).

[3] M. S. Senn, D. A. Keen, T. C. A. Lucas, J. A. Hriljac, and A. L. Goodwin, Phys. Rev. Lett. **116**, 207602 (2016).

[4] D. Nuzhnyy, S. Kamba, P. Kužel, S. Veljko, V. Bovtun, M. Savinov, J. Petzelt, H. Amorín, M. E. V. Costa, A. L. Kholkin, Ph. Boullay, and M. Adamczyk, Phys. Rev. B **74**, 134105 (2006).

[5] J. M. Perez-Mato, P. Blaha, K. Schwarz, M. Aroyo, D. Orobengoa, I. Etxebarria, and A. García, Phys. Rev. B **77**, 184104 (2008).

[6] W. S. Choi and H. N. Lee, Phys. Rev. B **91**, 174101 (2015).

[7] B. H. Park, B. S. Kang, S. D. Bu, T. W. Noh, J. Lee, and W. Jo, Nature (London) **401**, 682 (1999).

[8] C. Chiritescu, D. G. Cahill, N. Nguyen, D. Johnson, A. Bodapati, P. Keblinski, and P. Zschack, Science **315**, 351 (2007).

[9] E. J. Nichols, J. W. J. Shi, A. Huq, S. C. Vogel, and S. T. Misture, J. Solid State Chem. **197**, 475 (2013).

[10] J. H. Lee, R. H. Shin, and W. Jo, Phys. Rev. B **84**, 094112 (2011).

[11] A. Shrinagar, A. Garg, R. Prasad, and S. Auluck, Acta Crystallogr. Sec. A **64**, 368 (2008).

[12] Q. Zhou, B. J. Kennedy, and C. J. Howard, Chem. Mater. **15**, 5025 (2003).

[13] M. Iwata, K. Ando, M. Maeda, and Y. Ishibashi, J. Phys. Soc. Jpn. **82**, 025001 (2013).

[14] M. Kempa, P. Kuzel, S. Kamba, P. Samoukhina, J. Petzelt, A. Garg, and Z. H. Barber, J. Phys.: Condens. Matter **15**, 8095 (2003).

[15] D. K. George, A. Charkhesht, and N. Q. Vinh, Rev. Sci. Instrum. **86**, 123105 (2015).

[16] N. Q. Vinh, M. S. Sherwin, S. J. Allen, D. K. George, A. J. Rahmani, and K. W. Plaxco, J. Chem. Phys. **142**, 164502 (2015).

[17] P. Juhas, T. Davis, C. L. Farrow, and S. J. L. Billinge, J. Appl. Crystallogr. **46**, 560 (2013).
[18] Y. Yasuhiro, K. Shinji, and M. Jun'ichiro, Jpn. J. Appl. Phys. **45**, 7556 (2006).
[19] A. D. Rae, J. G. Thompson, R. L. Withers, and A. C. Willis, Acta Crystallogr. Sec. B **46**, 474 (1990).
[20] W. Kohn and L. J. Sham, Phys. Rev. **140**, A1133 (1965).
[21] P. Hohenberg and W. Kohn, Phys. Rev. **136**, B864 (1964).
[22] J. P. Perdew, K. Burke, and M. Ernzerhof, Phys. Rev. Lett. **77**, 3865 (1996).
[23] P. E. Blöchl, Phys. Rev. B **50**, 17953 (1994).
[24] G. Kresse and D. Joubert, Phys. Rev. B **59**, 1758 (1999).
[25] G. Kresse and J. Furthmüller, Comput. Mater. Sci. **6**, 15 (1996).
[26] G. Kresse and J. Furthmüller, Phys. Rev. B **54**, 11169 (1996).
[27] J. Min Ku, K. Yong-Il, N. Seung-Hoon, S. Jung Min, J. Chang Hwa, and W. Seong Ihl, J. Phys. D **40**, 4647 (2007).
[28] D. J. Singh, S. S. A. Seo, and H. N. Lee, Phys. Rev. B **82**, 180103 (2010).
[29] S. Baroni and R. Resta, Phys. Rev. B **33**, 7017 (1986).
[30] A. Togo and I. Tanaka, Scr. Mater. **108**, 1 (2015).
[31] R. Machado, M. G. Stachiotti, R. L. Migoni, and A. H. Tera, Phys. Rev. B **70**, 214112 (2004).
[32] See Supplemental Material at http://link.aps.org/supplemental/10.1103/PhysRevB.96.134114 for animated gif files of the phonon modes.
[33] D. Maurya, Y. Zhou, Y. Yan, and S. Priya, J. Mater. Chem. C **1**, 2102 (2013)
[34] F. K. Lotgering, J. Inorg. Nucl. Chem. **9**, 113 (1959).
[35] N. Q. Vinh, S. J. Allen, and K. W. Plaxco, J. Am. Chem. Soc. **133**, 8942 (2011).
[36] D. K. George, A. Charkhesht, O. A. Hull, A. Mishra, D. G. S. Capelluto, K. R. Mitchell-Koch, and N. Q. Vinh, J. Phys. Chem. B **120**, 10757 (2016).